NANO · MICRO small
www.small-journal.com

Enhancement of Mass Transport for Oxygen Reduction Reaction Using Petal-Like Porous Fe-NC Nanosheet

Chunfeng Shao, Shiguang Zhuang, Haocheng Zhang, Qike Jiang, Xiaoyan Xu, Jianshan Ye, Baitao Li, and Xiujun Wang**

Nitrogen-coordinated single-atom catalysts (SACs) have emerged as a new frontier for accelerating oxygen reduction reaction (ORR) owing to the optimal atom efficiency and fascinating properties. However, augmenting the full exposure of active sites is a crucial challenge in terms of simultaneously pursuing high metal loading of SACs. Here, petal-like porous carbon nanosheets with densely accessible Fe-N$_4$ moieties (FeNC-D) are constructed by combining the space-confinement of silica and the coordination of diethylenetriaminepentaacetic acid. The resulted FeNC-D catalyst possesses an enhanced mesoporosity and a balanced hydrophobicity/hydrophilicity, which can facilitate mass transport and advance the exposure of inaccessible Fe-N$_4$ sites, resulting in efficient utilization of active sites. By virtue of the petal-like porous architecture with maximized active site density, FeNC-D demonstrates superior ORR performance in a broad pH range. Remarkably, when utilized as the air cathode in Zn-air battery (ZAB) and microbial fuel cell (MFC), the FeNC-D-based device displays a large power density (356 mW cm^{-2} for ZAB and 1041.3 mW m^{-2} for MFC) and possesses remarkable stability, substantially outperforming the commercial Pt/C catalyst.

1. Introduction

Developing highly efficient and durable cathodic oxygen reduction reaction (ORR) electrocatalysts is of paramount significance for the successful implementation of emerging electrochemical energy technologies, for example, fuel cells and metal-air batteries.[1,2] An ideal cathode is expected to follow a four-electron pathway (e.g., $O_2 + 4H^+ + 4e^- \rightarrow 2H_2O$) with high catalytic activity, high durability, and low fabrication and material cost. Despite the most prominent ORR activity of Pt-based catalyst,[3] its high cost and vulnerability have motivated the exploration of active and durable non-precious metal catalysts.[4] Recently, the heteroatom (N, B, S, P, and F)-doped electrocatalysts have been developed with desirable ORR activity and the capability of being modified with metallic nanoparticles of transition metals (Mn, Ni, Co, and Fe, etc.).[5–7] These metal centers vastly affected the electron-transfer pathway in the ORR process. For instance, the Fe center usually produced a typical four-electron pathway with lower hydrogen peroxide yield, compared with other transition metals (Co, Ni, Mn, Cu, etc.).[8–10] Specifically, density functional theory calculations revealed that Fe-N$_x$ configuration exhibited strong adsorption capacity for O$_2$ and a lower energy barrier for subsequent O=O bond breaking,[11,12] which accelerated the ORR process. Compared to traditional catalysts, the single-atom catalysts (SACs), especially iron-nitrogen carbon (Fe-NC) with atomic Fe-N$_x$ moieties as principal active sites possess the merits of maximal atom utilization efficiency, extraordinary activity, and selectivity, as well as tunable electronic environments.[13,14] This class of electrocatalysts have been acclaimed as the frontier of advancing ORR.[15]

Recently, extensive researches have been conducted on Fe-NC single-atom catalysts (SACs) with dense Fe-N$_x$ active sites (metal loading of about 3 wt%).[16–18] Nevertheless, the balance between high iron loading and evenly dispersed atom is difficult to be optimized due to the migration and aggregation of Fe species during the thermal pyrolysis,[19,20] which causes high structural heterogeneity with relatively low-active Fe clusters/nanoparticles.[20–22] Furthermore, not all Fe-N$_x$ species are the active-sites for ORR owing to the different accessibility of metal sites. Most Fe-N$_x$ species are concentrated in the micropore of carbon support[23] and only 4.5% of Fe-N$_x$ sites can be utilized for catalyzing ORR.[24] Therefore, it is considered imperative to enhance the exposure of Fe-N$_x$ moieties and improve their utilization efficiency.

There are several strategies for enhancing the utilization of active sites in fuel cells. One powerful knob is increasing mesoporosity to form an efficient mass transfer channel for the inaccessible Fe-N$_x$ sites buried inside the dense 3D carbon skeleton.[16,25,26] Another approach is engineering thin carbon nanosheets with hierarchical porous structures to provide a large reaction interface area and sufficient metal site exposure.[8,27,28] Such unique architectures can facilitate electrolyte ions reservation and transport of reactants/products.[27,29] In order

---

C. Shao, S. Zhuang, H. Zhang, Prof. J. Ye, Prof. B. Li, Prof. X. Wang
Key Laboratory of Fuel Cell Technology of Guangdong Province
School of Chemistry and Chemical Engineering
South China University of Technology
Guangzhou 510640, China
E-mail: btli@scut.edu.cn; xjwangcn@scut.edu.cn
Dr. Q. Jiang, X. Xu
Dalian National Laboratory for Clean Energy
Dalian Institute of Chemical Physics
The Chinese Academy of Sciences
Dalian 116023, China

The ORCID identification number(s) for the author(s) of this article can be found under https://doi.org/10.1002/smll.202006178.

DOI: 10.1002/smll.202006178

to effectively control nanosheet configuration and aperture-structure, various templates (e.g., silica and NaCl) are introduced during synthesis.[8,29,30] Importantly, the confinement effect induced by silica template can mitigate aggregation of Fe species by reducing the surface energy of Fe atoms, and thus ensuring the stability of high-loading SACs.[16,18,31,32] Constructing proper hydrophobicity of the carbon surface is another resource to accelerate the mass-transport in the Fe-NC catalyst layer. Because a reasonable surface wettability on the catalyst surface can form a steady three-phase boundary, which will promote water removal and sufficient O_2 diffusion, and alleviate the performance degradation caused by water flooding in the cathode catalyst layer. Several strategies have been explored for tuning the wettability of air cathode, including increasing pyrolysis temperature,[33] surface fluorination,[34] and adding a hydrophobic substance (such as polytetrafluoroethylene,[35–37] polydimethylsiloxane,[38] macromolecule,[39] and SiO_2 chains).[40] Nevertheless, these methods inversely reduce the intrinsic activity or increase ion diffusion limitation and electrical impedance. Hence, integrated tactics, namely controlling nanosheet-like configuration, mesoporosity, and surface hydrophobicity hold great promise for elevating the availability of Fe-N_x moieties without lowering the intrinsic activity of the catalyst.

In this work, a versatile silica-confined strategy to build petal-like porous carbon nanosheets with high mesoporosity and appropriate hydrophobicity to substantially facilitate the mass transfer was developed. Thereinto, a novel coordinated iron complex derived from diethylenetriaminepentaacetic acid (DTPA) and melamine was prepared and subsequently pyrolyzed into Fe-NC material. Owing to the strong coordination of DTPA and confinement effect of silica, the encapsulated Fe atoms could be effectively isolated and anchored during annealing treatment, achieving the isolation of Fe atoms embedded nanosheet. Meanwhile, the carbon nanosheet featured dense Fe-N_4 active sites, high nitrogen content, and abundant defects could deliver numerous active sites. Besides the architectural and compositional merits, the as-fabricated Fe-NC SAC (FeNC-D0.5) can expose the originally inaccessible sites and maximize their utilization for advanced catalytic ORR in a pH-universal medium. Furthermore, when the FeNC-D0.5 was employed as the air cathode catalyst in Zn-air battery (ZAB) and microbial fuel cell (MFC), both devices achieved remarkable power density (356 mW cm^{-2} and 1041.3 mW m^{-2}, respectively).

2. Results and Discussion

The overall synthesis for the petal-like structured atomically dispersed Fe-NC catalyst was briefly illustrated in **Figure 1**a. First, mesoporous silica nanoparticle (MSN) templates with

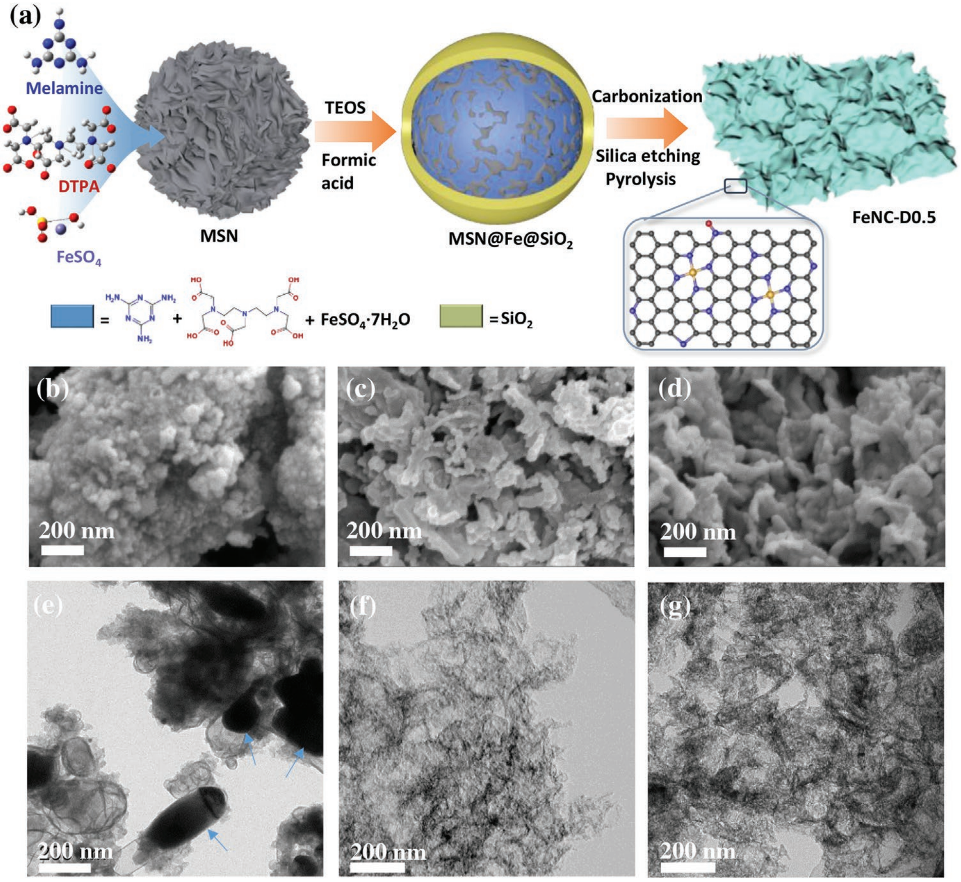

Figure 1. a) Schematic illustration for the preparation of FeNC-D0.5 catalyst; SEM images of b) FeNC-D0, c) FeNC-D0.5, and d) FeNC-D1; TEM images of e) FeNC-D0, f) FeNC-D0.5, and g) FeNC-D1.

$AlCl_3$-grafting were filled and coated with melamine, DTPA, and Fe^{2+}, followed by depositing silica layer (MSN@Fe@SiO_2) and heat-treatment. After silica etching and pyrolysis, the atomically Fe dispersed N-doped porous carbons (FeNC-D0.5) was synthesized. Specifically, the melamine and DTPA contained abundant amine functional groups and carboxylic acid groups, which could strongly bind with iron ions via coordination interactions to form an iron complex, contributing to the formation of electrochemically active metal nitrogen moieties. With the existence of Al^{3+}, the complex precursor was readily adsorbed on the porous surfaces of MSN, and thus filling the template. Subsequently, these amino groups and carbonyl groups reacted with each other via the Schiff base reaction at high temperature.[41] Meanwhile, the crosslinking of the as-formed chains was promoted by the chelated metal ions.[32,41] Combining the confinement effect of silica template and overcoating, the retention and structure of decomposed intermediates were corroborated, making it an ideal candidate for constructing petal-like porous carbon sheets. To analyze the unique advantage of two nitrogen sources, FeNC-D1 catalyst with only DTPA and FeNC-D0 with only melamine were prepared using the same process. Furthermore, the function of MSN was validated by synthesizing another control catalyst (FeNC-D0.5-N) without the MSN template.

Scanning electron microscopy (SEM) images revealed the morphology change from the flower-like structure of MSN (**Figure 2**a) to the petal-like porous structure of FeNC-D0.5 (Figure 1c). Interestingly, the petaloid morphology was uniform and fluffy for FeNC-D1 (Figure 1d) but disappeared in FeNC-D0 where only the stacking of particles was observed (Figure 1b), indicating the presence of DTPA was beneficial for obtaining the petal-like structure. The porous structure (Figure S1a, Supporting Information) was well-retained in FeNC-D0.5-N, even in the absence of silica templates, implying the high pore-making ability for melamine and DTPA.

The transmission electron microscopy (TEM) image demonstrated that there was a large number of macropores and mesopores, which constituted interconnected network structures in the FeNC-D0.5 catalyst (Figure 1f). In addition to the porous network, more uniform petal-like nanosheets were distinctly observed in the FeNC-D1 catalyst (Figure 1g), coinciding with the topography in SEM image (Figure 1d). A high-resolution TEM image (Figure 2b,c) exhibited the amorphous structure in FeNC-D0.5, as well as numerous nanosized pores across its surface, which would produce various holes and edge defects.

It should be noted that no nanoparticles were found in the TEM images of FeNC-D0.5 and FeNC-D1. Meanwhile, the X-ray diffraction (XRD) patterns of FeNC-D0.5 and FeNC-D1 showed two low-intensity peaks at 29° and 42° with the respective planes of (002) and (100) for carbon[42–44] and no obvious signals for crystalline Fe species (Figure 2d), suggesting that

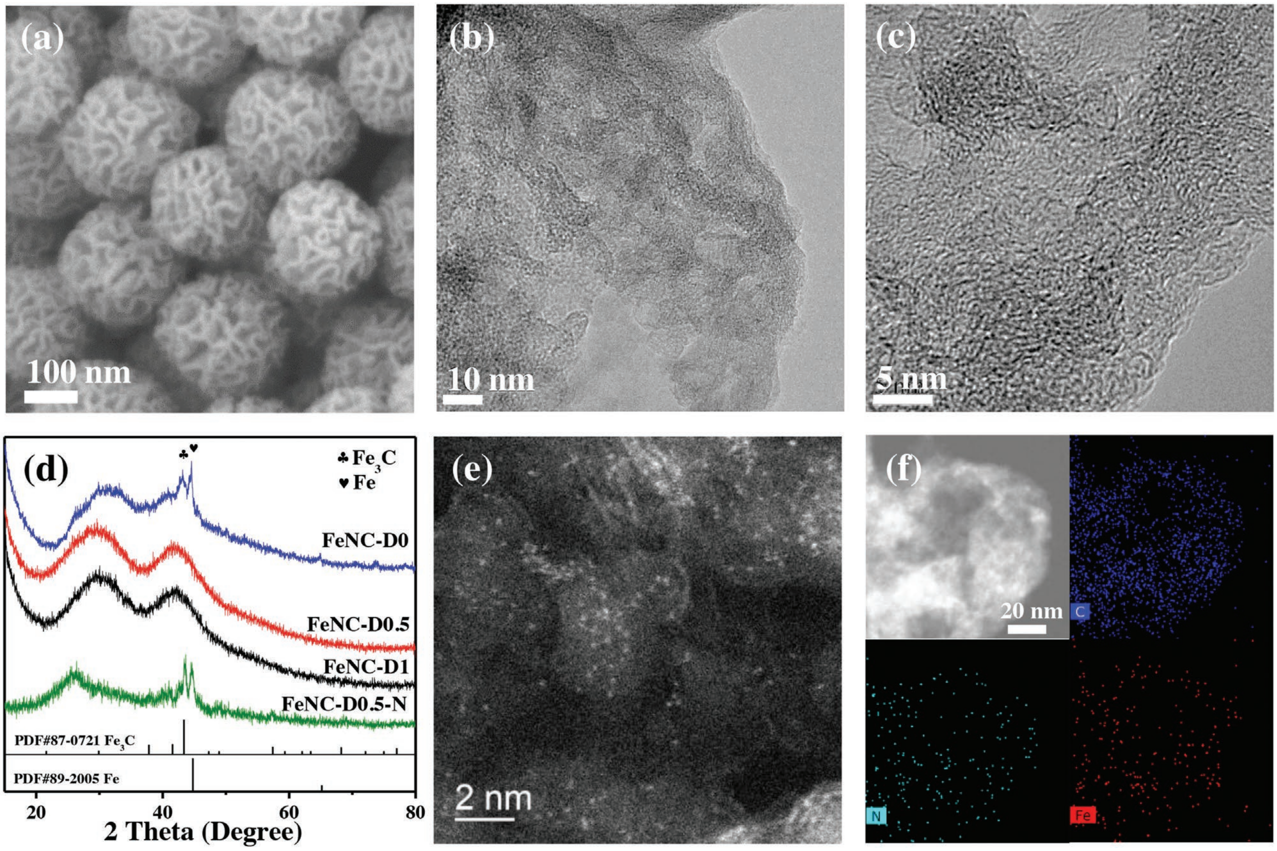

Figure 2. a) SEM image of MSN; b,c) HRTEM images of FeNC-D0.5; d) XRD pattern of FeNC-D*n*; e) Aberration-corrected HAADF-STEM image of FeNC-D0.5; f) HAADF-STEM image and corresponding element mappings of FeNC-D0.5.

Fe might exist in an atomic form.[20] By contrast, some large crystalline particles (marked with blue arrows) were observed in the FeNC-D0 catalyst (Figure 1e), which could be identified as Fe_3C compound and metallic Fe based on the XRD patterns (Figure 2d). Moreover, the hollow structures in the TEM image (Figure 1e) were typical hollow graphitic carbon shells produced via the catalysis of Fe-based particles as a graphitization agent, especially when melamine was used as a nitrogen precursor.[45,46] Similar to the melamine-derived catalyst, many small Fe-based nanoparticles were dispersed in the carbon phase for the FeNC-D0.5-N catalyst without MSN template (Figure S1b, Supporting Information, and Figure 2d). These results confirmed that DTPA exhibited higher dispersion ability and stronger coordination ability with metal ions compared to melamine. Meanwhile, after combined with the MSN template, FeNC-D0.5 inhibited the generation of Fe-based particles. Furthermore, the silica overcoating and acid treatment during the synthesis process were critical for inhibiting aggregation, as indicated by XRD results of control catalysts (Figure S2, Supporting Information). The sub-angstrom-resolution high-angle annular dark-field scanning TEM (HAADF-STEM) measurements (Figure 2e) were performed to corroborate the formation of isolated iron atoms in FeNC-D0.5. Corresponding to heavier Fe atoms, numerous individual bright dots uniformly dispersing throughout the carbon matrix were detected as the isolated atom format rather than clusters. Additionally, the homogeneous spatial distribution of C, N, and Fe elements on the entire nanostructure was confirmed by energy dispersive spectrum (EDS) mappings (Figure 2f).

X-ray absorption spectroscopy (XAS) was conducted to identify the chemical state and atomic coordination of single atomic Fe sites in FeNC-D0.5 (**Figure 3**a). The energy absorption threshold

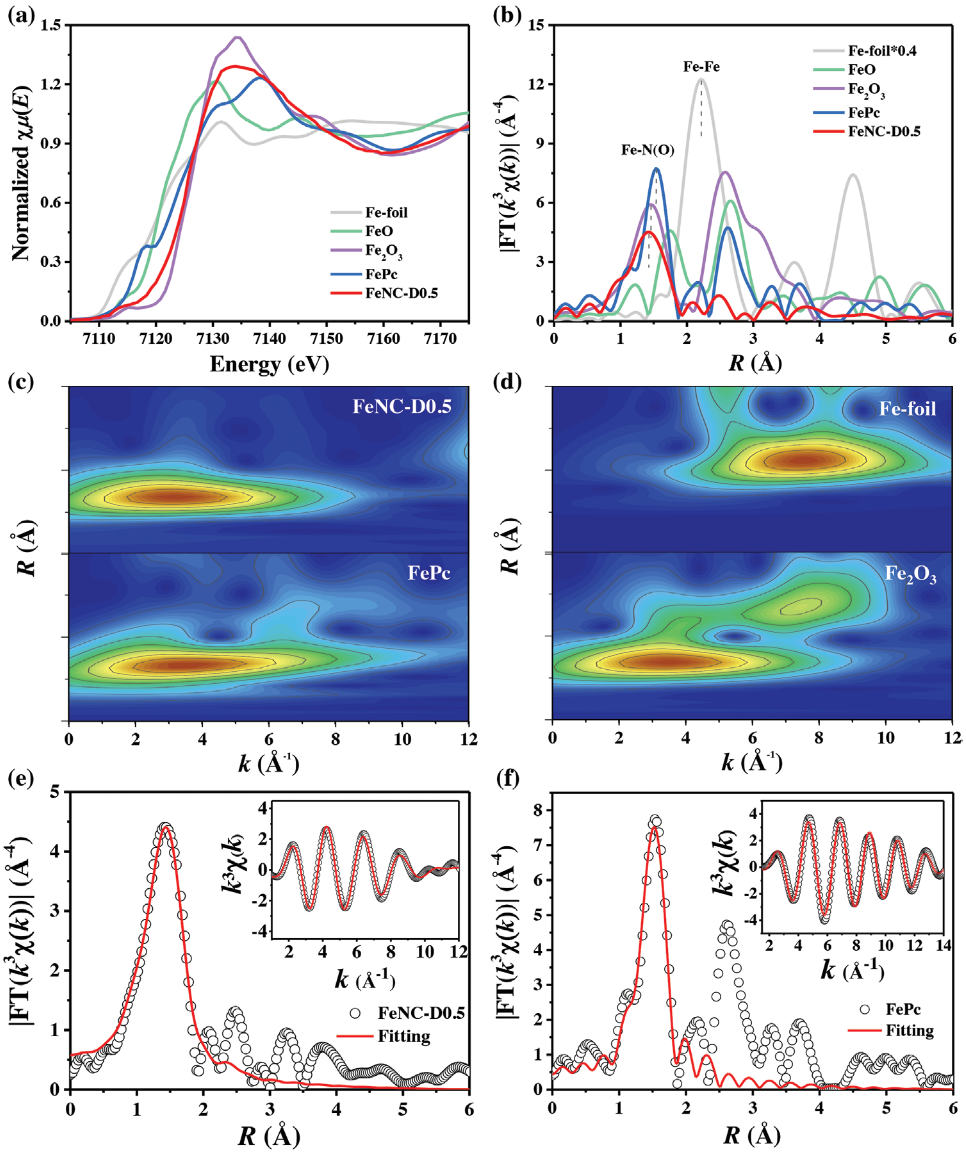

Figure 3. a) Fe K-edge XANES spectra and b) FT-EXAFS spectra for FeNC-D0.5, Fe-foil, FeO, Fe_2O_3, and FePc; c,d) Wavelet transform of Fe K-edge EXAFS for FeNC-D0.5 and references; EXAFS analysis of e) FeNC-D0.5 and f) FePc at *R* space (inset: the corresponding fitting curves in *k* space).

of X-ray absorption near edge structure (XANES) spectra of FeNC-D0.5 located between standard FeO and Fe_2O_3, elucidating the existence of the positive-charged Fe atoms ($2 < \delta < 3$). Fourier-transformed extended X-ray absorption fine structure (FT-EXAFS) profile of FeNC-D0.5 displayed a significant peak centered at ≈1.44 Å (Figure 3b), which was corresponded to Fe-N(O) first coordination shell and was analogous to the chemically defined FePc.[20,47,48] Compared to Fe-foil and Fe_2O_3 references, the Fe–Fe peak at ≈2.2 Å was not observed on FeNC-D0.5, confirming the atomic dispersion property of Fe. Furthermore, wavelet transform (WT) was performed to analyze Fe K-edge EXAFS oscillations, which can discriminate different atoms in the adjacent atomic layer.[21,49] Impressively, the WT cont3ur plot (Figure 3c,d) of FeNC-D0.5 presented only one intensity maximum at about 3.4 $Å^{-1}$, which was approximate to that of FePc reference (≈3.6 $Å^{-1}$) but quite distinct from the standard Fe foil (7.5 $Å^{-1}$) and Fe_2O_3 (3.5 and 7.5$Å^{-1}$). Consequently, Fe species existed as the mononuclear Fe centers rather than the crystalline structure. The quantitative chemical configurations of FeNC-D0.5 were acquired by fitting the FT curve of Fe K-edge EXAFS spectra in R space and k space (Figure 3e). The fitting parameters (Table S1, Supporting Information) revealed that the first shell peak at 1.44 Å was attributed to monodispersed Fe atom coordinated by four-fold N atoms (bond length 1.98 Å) as Fe-N_4 configuration, compared with the fitting result for FePc (Figure 3f). Besides, one absorbed O_2 molecule might exist in the axial direction of the Fe-N_4 plane.[25,26]

The degree of graphitization and disorder of the synthesized catalysts were further estimated by the Raman spectroscopy. Two prominent peaks situated at 1595 (G band) and 1352 cm^{-1} (D band) (**Figure 4**a) could be attributed to the vibration of sp^2-hybridized carbon atoms and structural defects such as disorders, holes, and edge defects,[50,51] respectively. The intensity ratios of I_D/I_G for FeNC-D0, FeNC-D0.5, and FeNC-D1 were 1.01, 1.05, and 1.06, respectively, signifying an increasing disorder degree and a decreasing graphitization degree with DTPA content. The higher ratio of I_D/I_G (1.15) in FeNC-D0.5-N revealed that DTPA accelerated the formation of a large number of defects in the absence of the MSN template.

The pore properties of the obtained catalysts were evaluated by nitrogen adsorption/desorption isotherm measurements. All catalysts exhibited typical type-IV isotherms with notable Type H3 hysteresis (Figure 4b), demonstrating the presence of mesoporosity.[52] Specifically, in the FeNC-D0.5 and FeNC-D1 catalysts, the hysteresis loops rose steadily with P/P_0, which was usually regarded as the characteristic of the flake structures.[53,54] These flake structures were also confirmed in the SEM images (Figure 1c,d). The Brunauer–Emmett–Teller (BET) surface areas, pore volume, and pore sizes for the prepared catalysts were summarized in Table S2, Supporting Information. FeNC-D0.5 displayed approximately double the specific surface area (SSA, 698 $m^2\ g^{-1}$) as large as the MSN template (333 $m^2\ g^{-1}$), implying the formation of highly porous structure as the result of decomposition of iron complex

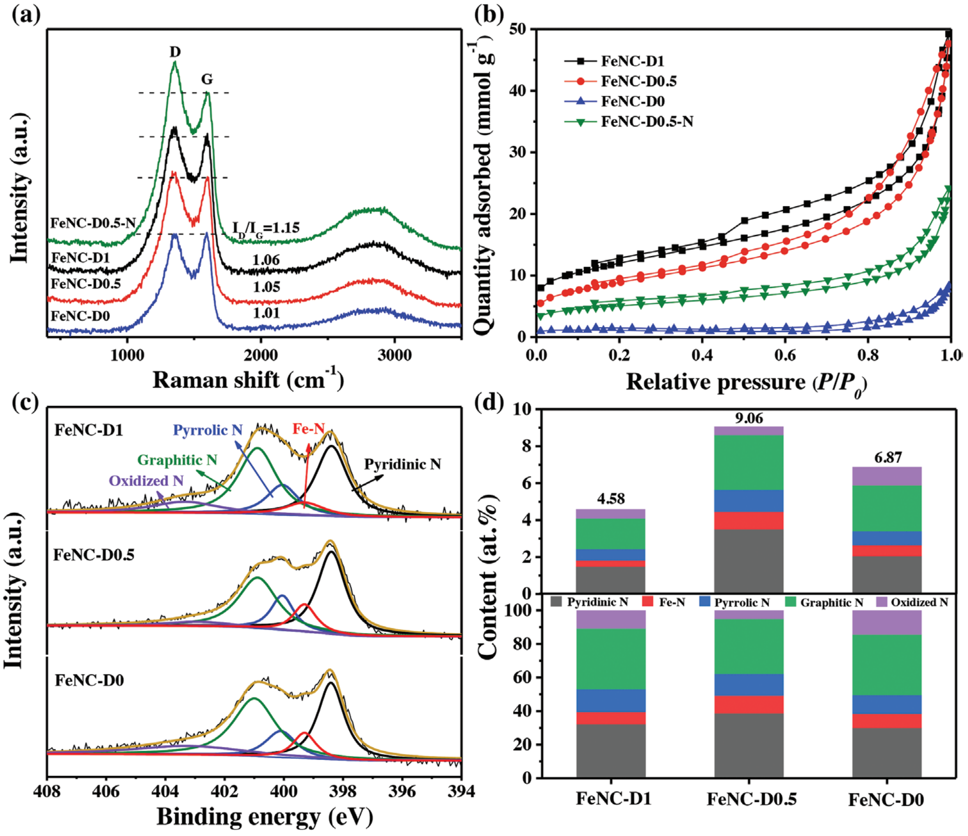

Figure 4. a) Raman spectra; b) nitrogen adsorption/desorption isotherms; c) high-resolution N 1s XPS spectra; d) atomic contents (up) and relative ratios (down) of the deconvoluted N species for the FeNC-D*n* materials.

confined in the silica framework. The SSA was 922 m^2 g^{-1} for the FeNC-D1 catalyst and 64 m^2 g^{-1} for the FeNC-D0 catalyst. In addition, the pore size distributions revealed the mesoporous structure (Figure S3a, Supporting Information), and the average pore diameter (APD) was larger than 5 nm (Table S2, Supporting Information). With the elevation of DTPA addition, the pore size distribution widened and the APD lessened. The higher SSA and porous structure with DTPA content implied that DTPA was conductive to the formation of highly-developed porosity. Compared with melamine, DTPA played a vital role in optimizing the porosity and morphology, which was possibly caused by the unique 3D molecular structure and the release of more volatile molecules from the DTPA derivative during the high-temperature pyrolysis.[55] Particularly, the external surface area was predominant in all catalysts (>70%, Table S2, Supporting Information), with FeNC-D0.5 possessing the highest proportion of 91% and the highest pore volume of 1.34 cm^3 g^{-1} (Table S2, Supporting Information) among the FeNC-D*n*.

X-ray photoelectron spectroscopy (XPS) was used to investigate the chemical composition and state of the specific elements in FeNC-D*n* catalysts. The XPS survey of FeNC-D0.5 revealed the existence of C, N, Fe, O, and S species (Figure S4a, Supporting Information), while no Al species were detected. The corresponding atomic surface concentrations (Table S2, Supporting Information) showed the N content in FeNC-D0.5 was 9.06 at%, higher than that of FeNC-D1 (4.58 at%) and FeNC-D0 (6.87 at%), suggesting that the combination of DTPA and melamine significantly promoted the content of nitrogen. This was attributed to the ultrahigh nitrogen content of melamine and the absence of crystalline Fe species, the latter was beneficial for improving the graphitization degree but reducing nitrogen content.[45] The high-resolution N1*s* spectra (Figure 4c) were deconvoluted into five component peaks at the binding energies of 398.4, 399.3, 400.0, 400.9, and 402.9 eV, which could be ascribed to pyridinic N, Fe-N, pyrrolic N, graphitic N, and oxide N, respectively.[19,20,45,56,57] The fitting results (Figure 4d and Table S3, Supporting Information) unveiled that, the pyridinic N and graphitic N were predominant in all catalysts. These doping-derived sites were expected to serve as the active sites for ORR, since pyridinic-N species are critical for facilitating electron transfer and lowering overpotential.[58,59] Meanwhile, graphitic N atoms can improve the four-electron catalytic pathway.[60–62] Total Fe content and the concentration of nitrogen coordinated with Fe (Fe-N$_x$) in FeNC-D0.5 were higher than those in FeNC-D1 and FeNC-D0, implying a positive correlation with the N doping level. Furthermore, Fe 2p spectrum of FeNC-D0.5 (Figure S4b, Supporting Information) revealed doublet peaks for Fe^{2+} (710.6 and 724.1 eV) and Fe^{3+} (713.7 and 726.6 eV), and no signal for metallic Fe was detected (≈707.3 and ≈720.2 eV).[19,48,60]

The surface wettability of FeNC-D*n* materials was investigated using contact angle measurement. All the FeNC-D*n* catalysts exhibited a good hydrophobicity with contact angle larger than 90° (**Figure 5**). The contact angle generally increased with a higher DTPA proportion. Specifically, at 0 s, the initiating contact angle increased from 114.3° for FeNC-D0 to 137.5° for FeNC-D1, and the latter was close to the superhydrophobic state (defined as contact angle higher than 145°). After 400 s, the water contact angle of FeNC-D1 dropped slightly to 135.8° (Figure 5a) and that of FeNC-D0.5 decreased

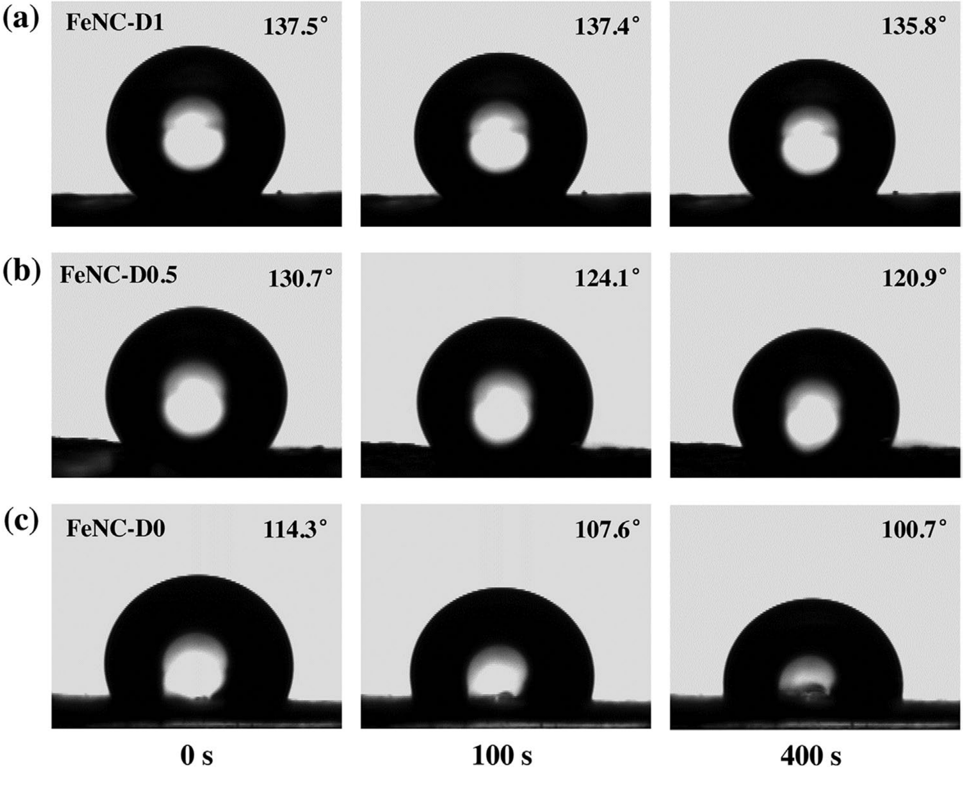

Figure 5. a–c) Dynamic imaging of water droplets on FeNC-D*n* catalysts.

moderately to 120.9° (Figure 5b), while the contact angle of FeNC-D0 decreased substantially to 100.7° (Figure 5a), suggesting the low surface hydrophobicity for FeNC-D0. Although the increasing DTPA content diminished the graphitization degree (Figure 4a), the FeNC-D*n* catalysts displayed a gradually upward hydrophobicity, demonstrating that the beneficial role of the thin petal-like structure effectively increased the surface tension of water[63] and balanced the hydrophobicity and hydrophilicity.[64] Therefore, the FeNC-D0.5 catalyst well integrated the fluffy petaloid structure for suppressing stack and nanosheets agglomeration, the abundant meso/macropore for shortening molecule/ion diffusion distance, and the balanced hydrophobic/hydrophilic surface for accelerating water removal, oxygen diffusion, and maintaining ion conductivity. All of these features maximized mass transport throughout the whole electrode.

The electrocatalytic activities of FeNC-D*n* were measured by a rotating disk electrode (RDE) technique in the O_2-saturated alkaline, neutral, and acidic solutions, respectively. As shown in **Figure 6**a,d and Table S4, Supporting Information, the half-wave potential ($E_{1/2}$) of FeNC-D0.5 was approximately 0.866 V, which was distinctly better than that of commercial Pt/C (0.845 V), FeNC-D1 (0.830 V), FeNC-D0 (0.825 V), and FeNC-D0.5-N (0.829 V) in 0.1 M KOH. This result indicated that the unique Fe-NC porous carbon networks possessed both outstanding structural and compositional advantages, and thus advancing catalytic ORR. The ultrahigh diffusion-limited current density (J_L) of about 6.63 and 6.40 mA cm^{-2} could be detected in FeNC-D0.5 and FeNC-D1 catalyst, respectively, massively exceeding that of FeNC-D0, Pt/C, and other ORR catalysts previously reported (Table S5, Supporting Information), which could be attributed to the excellent water/air catalytic interface for high-efficiency mass transfer induced by large SSA, proper hydrophobicity, and fluffy petaloid morphology. However, the LSV curve of FeNC-D1 catalyst was more negative than FeNC-D0.5 due to insufficient active sites, revealing that a high density of atomic Fe sites generated plentiful active sites associated with the augmented activity. The optimal FeNC-D0.5 catalyst also exhibited the highest $E_{1/2}$ of 0.692 V in 0.05 M PBS (Figure 6b,e), which was about 62 mV positive relative to that of Pt/C catalyst. This $E_{1/2}$ value was 42, 69, and 20 mV higher than that of FeNC-D1, FeNC-D0, and FeNC-D0.5-N, respectively. In addition, the FeNC-D0.5 was endowed with respectable ORR activity in 0.5 M H_2SO_4, surpassing other control catalysts, and was close to that of Pt/C in 0.1 M $HClO_4$ (Figure 6c,f). The electrochemical performance of FeNC-D0.5 in pH-universal media was comparable to non-noble metal catalysts recently reported (Tables S5, Supporting Information), implying its excellent catalytic activity toward ORR.

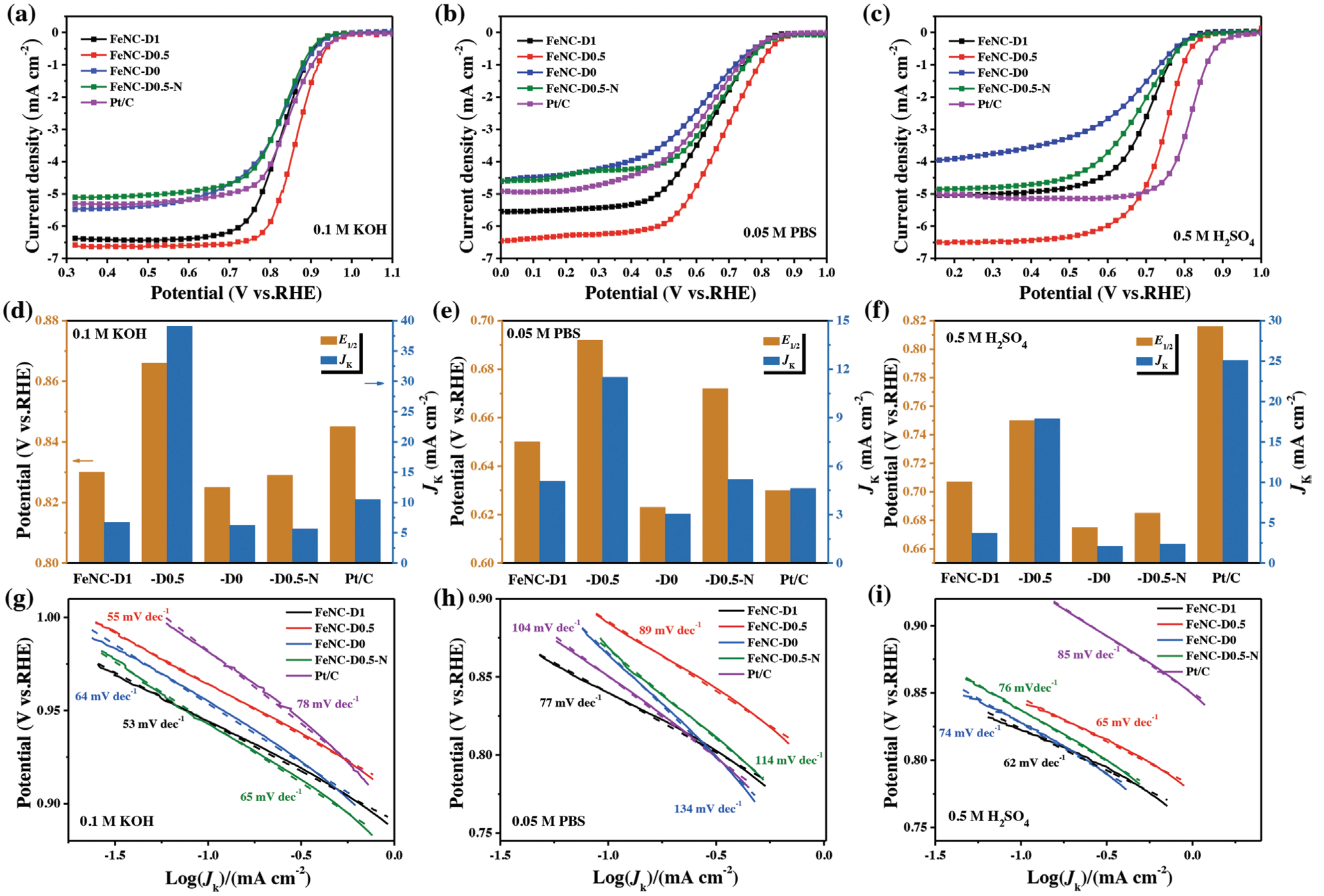

Figure 6. a–c) LSV curves of FeNC-D*n* catalysts and Pt/C at a rotation rate of 1600 rpm in O_2-saturated 0.1 M KOH, 0.05 M PBS, and 0.5 M H_2SO_4 solution (0.1 M $HClO_4$ for Pt/C); d–f) Corresponding half-wave potentials and kinetic current density at different potentials, and g–i) Tafel plots of FeNC-D*n* and Pt/C catalysts.

To better quantitatively compare catalytic activities, the kinetic current density (J_k) at different potentials by the Koutecky–Levich equation were compared (Figure 6d–f and Table S4, Supporting Information). the J_k of FeNC-D0.5 was approximately 39.11 mA cm^{-2} in 0.1 M KOH at 0.8 V, vastly exceeding that of FeNC-D1 (6.73 mA cm^{-2}), FeNC-D0 (6.25 mA cm^{-2}), FeNC-D0.5-N (5.66 mA cm^{-2}), as well as the Pt/C catalyst (10.48 mA cm^{-2}). In 0.05 M PBS solution, the FeNC-D0.5 exhibited a large J_k (11.50 mA cm^{-2}) at 0.6 V, outperforming the reference catalysts and Pt/C (Figure 6e). These results supported that electrocatalytic activities of FeNC-D0.5 in alkaline and neutral solutions were far superior to those of the control catalysts and commercial Pt/C catalyst. In acidic solution, the J_k of FeNC-D0.5 reached 17.86 mA cm^{-2} at 0.7 V close to that of Pt/C (Figure 6f).

As the introduction of the DTPA and MSN template most likely enabled the catalyst with high porosity and more active sites, the electrochemical surface area (ECSA) of the as-prepared catalysts was evaluated to compare the exposed active site density. The ECAS was generally proportional to the electrochemical double-layer capacitance (C_{dl}) that could be obtained using the cyclic voltammetry at various scanning rates (Figure S5a–d, Supporting Information). FeNC-D0.5 displayed the highest ECSA value (C_{dl} of 88.5 mF cm^{-2}) among these catalysts (Figure S5e, Supporting Information), even though it's SSA was lower than that of FeNC-D1, suggesting that FeNC-D0.5 catalyst possessed the high density and superb accessible active sites. The unique petaloid structure with abundant meso/macropores, high pore volume and SSA in FeNC-D0.5 could accommodate dense active sites and accelerate mass transport pathway, and thus boosting the active site density.[16] Furthermore, the Tafel curves of all the catalysts were plotted based on the polarization curves after mass-transport correction in order to evaluate the kinetic of these electrocatalysts for ORR (Figure 6g–i). At the low over-potential, the calculation results revealed that FeNC-D0.5 possessed the Tafel slopes of 55, 89, and 65 mV dec^{-1} in alkaline, neutral, and acidic media, respectively. These values were much lower than those of FeNC-D0 and FeNC-D0.5-N, even better than Pt/C, and similar to those of FeNC-D1, confirming that the class of catalysts had high intrinsic ORR activity, even in the case of the FeNC-D1 catalyst with the extremely low content of Fe-N$_x$ species (according to the XPS result). Furthermore, the poor performance such as relatively negative $E_{1/2}$, small J_k, and large Tafel slope of FeNC-D0 and FeNC-D0.5-N probably originated from the aggregation of Fe atoms and the loss of active sites. Compared with these Fe-based catalysts, the combination of densely active Fe-N$_x$ species and nitrogen-rich porous carbon structure in the FeNC-D0.5 catalyst offered numerous active sites with adequate exposure, resulting in highly efficient ORR.

Furthermore, ORR catalytic behaviors were assessed by calculating the yield of peroxide species (HO_2^-) and transferred electron number (n) based on the rotating RDE (RRDE) measurements. The HO_2^- yield over the FeNC-D0.5 catalyst was below 4.0% in the over-potential region of 0.3–0.9 V versus RHE, and n was the range of 3.92–3.98 (**Figure 7**a), implying the reduction catalysis proceeded dominantly via a four-electron pathway in the alkaline medium. Meanwhile, the effective 4e reduction pathway for the FeNC-D0.5 electrode also occurred in a neutral electrolyte, evidenced by the low HO_2^- yield (≈1.2% at 0.4 V) and large n (≈3.97) (Figure 7b). Except for in the acidic media (Figure 7c), the reaction pathway for FeNC-D0.5 was superior to the Pt/C electrode in both alkaline and neutral media.

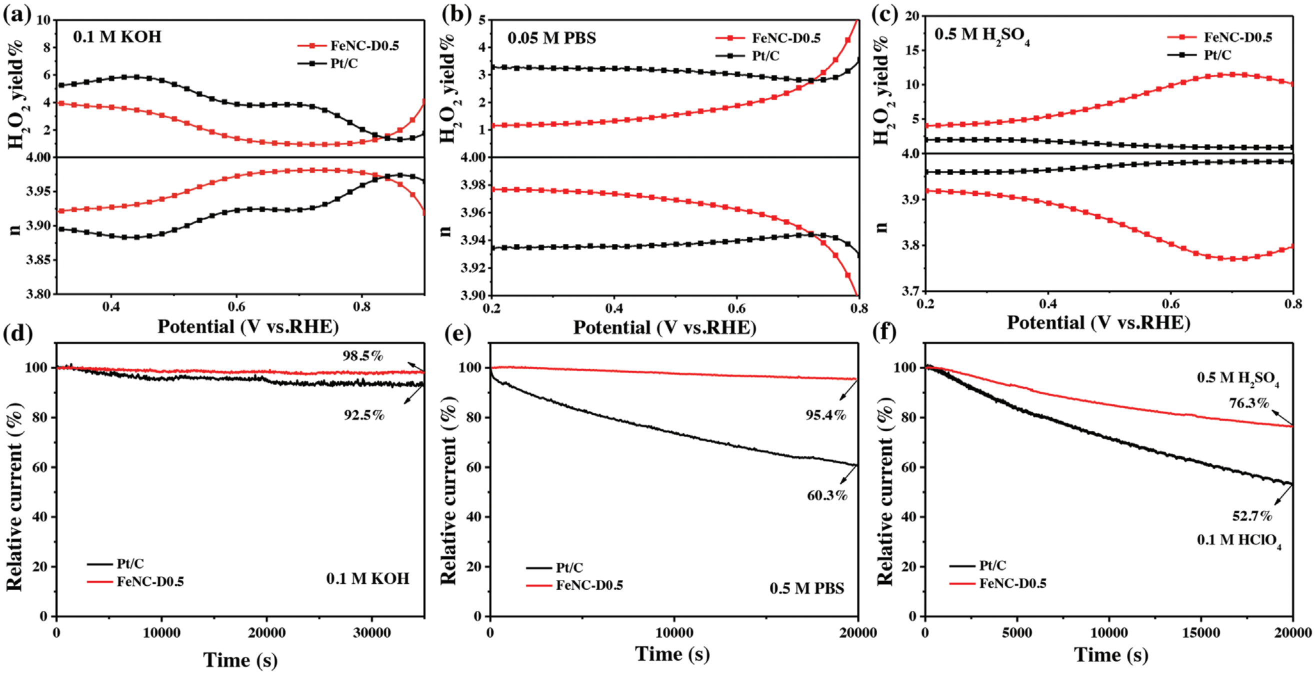

Figure 7. a–c) HO_2^- and calculated electron transfer number of FeNC-D0.5 and Pt/C in different solutions. d–f) The CP response of FeNC-D0.5 and Pt/C at 0.7 V.

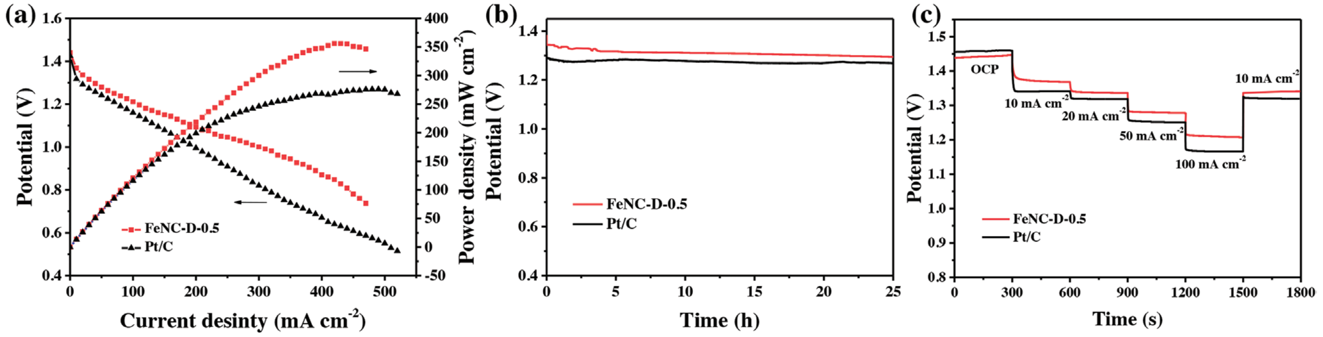

Figure 8. a) Polarization and power density plots of the ZABs using FeNC-D0.5 and Pt/C catalysts; Corresponding galvanostatic discharge curves at b) 10 mA cm^{-2} and c) different current densities.

High ORR activity of FeNC-D0.5 was further supported by comparing their electrocatalytic stability and methanol tolerance, which are part of the main obstacles for fuel cell catalysts in commercial applications.[65] The durability of FeNC-D0.5 and Pt/C catalysts was evaluated by means of a chronoamperometric (CP) measurement at 0.7 V in all-pH solutions saturated with O_2. FeNC-D0.5 catalyst exhibited the attenuation rate of only 1.5% in alkaline medium, 4.6% in neutral medium, and 23.7% in acid medium (Figure 7d–f), meanwhile, the corresponding decay in $E_{1/2}$ were shown in Figure S6a–c, Supporting Information. The results revealed that the stability of the FeNC-D0.5 electrode gradually descended as the pH value dropped, but still outperformed the Pt/C electrode. The reason for the promising stability of FeNC-D0.5 is that the strong interaction between the isolated Fe atoms and N-doping carbon nanosheets could restrain the migration and aggregation of the active sites. The considerable difference of stability between FeNC-D0.5 and Pt/C probably arose from the adsorption of phosphate anions in the active Pt sites in a neutral solution.[66] Furthermore, the FeNC-D0.5 catalyst displayed exceptional immunity to methanol crossover. After adding methanol in the CP test (Figure S7, Supporting Information), only slight fluctuations in current and $E_{1/2}$ were observed for FeNC-D0.5, while Pt/C catalyst suffered a sharp decline. These electrochemical data revealed that FeNC-D0.5 could be used as an efficient catalyst with superior ORR activity and methanol durability.

To evaluate the application of as-prepared catalyst in energy conversion devices, the primary ZABs with FeNC-D0.5 as the air cathode (loading of 4 mg cm^{-2}) and Zn power as the anode in 6.0 м KOH were assembled. For comparison, the ZAB based on the commercial 20 wt% Pt/C was also assembled under the same condition. The ZAB driven by FeNC-D0.5 delivered an impressive peak power density of 356 mW cm^{-2} at a current density of 420 mA cm^{-2} (**Figure 8**a), which was about 1.3 times higher than that of the Pt/C-based device (276 mW cm^{-2}) and outperformed most of the previously reported non-precious-metal catalysts (Table S5, Supporting Information). The galvanostatic discharge profile (Figure 8b) of the FeNC-D0.5-based battery exhibited a steady voltage of 1.30 V at 10 mA cm^{-2} and no visible degradation throughout the entire test period, denoting the substantial durability and the practical potential of the FeNC-D0.5 catalyst. Besides, the current density was further altered between 0 and 100 mA cm^{-2} to assess the stability of cycle discharge performance. With elevating current densities, the potential plateaus (Figure 8c) of the FeNC-D0.5 equipped device fell, but were still higher than those of the battery equipped with Pt/C, especially at high current density, which was mainly attributed to the efficient utilization of Fe-N_4 moieties in the FeNC-D0.5 catalyst. The hydrophobic catalyst surface along with a petal-like hierarchical porous structure vividly boosts the water transport and improves the accessibility of Fe-N_4 active sites for oxygen, and thus mitigating the negative impacts caused by water flooding.[67] These results stated FeNC-D0.5 as an admirable catalyst to substitute Pt/C catalyst for ZAB.

In addition, the power generation of MFCs using FeNC-D0.5 as the air cathode was assessed in order to expand the application in neutral media. Single-chamber MFCs (SCMFC, **Figure 9**a) can recover the biomass energy into renewable electricity, in which electroactive microbes in the wastewater can oxidize organic matter and the generated transfer electrons flow to the cathode by the circuit, where O_2 is reduced upon the catalysis process.[68,69] The FeNC-D0.5 cathode and Pt/C control cathode were assembled individually into SCMFCs equipped with the same anode and fed with the same sewage medium to minimize the impact of anode exoelectrogens on the polarization curve. The polarization curves and power outputs (Figure 9b) showed that the FeNC-D0.5-MFC delivered a maximum power density of 1041.3 mW m^{-2}, which was 47.8% higher than that of Pt/C-MFC (704.6 mW m^{-2}) and comparable to the non-noble ORR catalysts previously reported (Table S5, Supporting Information). The durability of FeNC-D0.5-MFC was also evaluated by monitoring the voltage output over about 800 h (Figure 9c). Though the voltage output of Pt/C-MFC (561 mV) was higher than that of FeNC-D0.5-MFC (539 mV) in the 1st cycle, it noticeably declined to ≈458 mV in the 6th period due to sulfide or chloride poisoning and biofilm growth.[70] Nevertheless, the attenuation for FeNC-D0.5-MFC was much gentle (only 20 mV), implying the good stability of the FeNC-D0.5 cathode. Besides, the polarization curves (Figure S8, Supporting Information) of the cathode followed the same trend as the cell voltage, and anode voltages behaved similarly in all SCMFCs tested, suggesting the variation in the MFC performances was mainly attributed to the different ORR activity of the cathode catalysts. On the whole, the petal-like carbon nanosheet with a uniform dispersion of FeN_4 sites exhibited the superior ORR catalytic activity and durability to improve MFC performance.

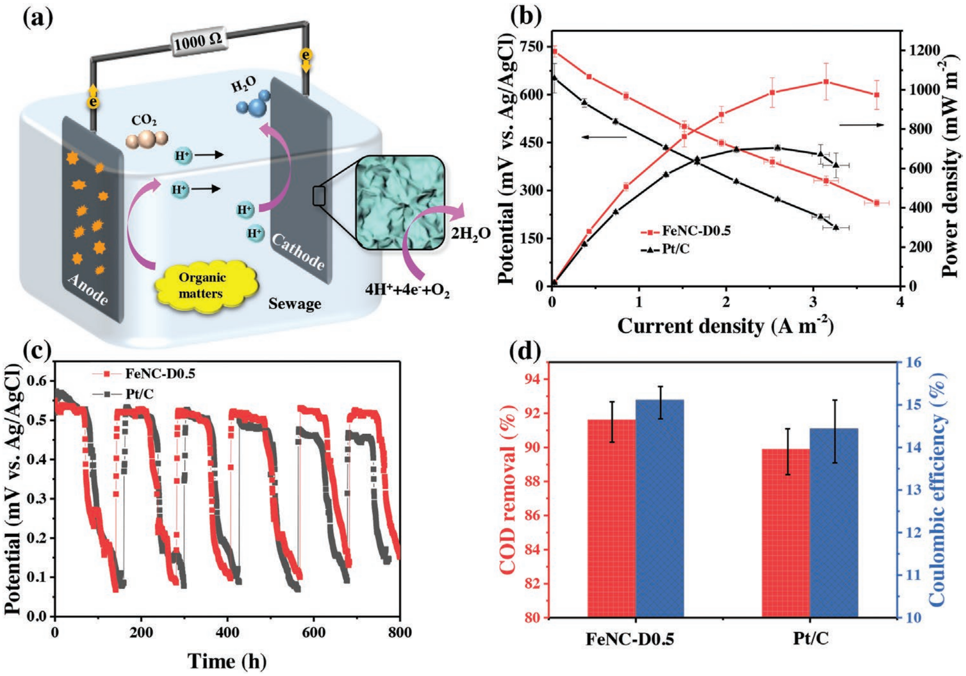

Figure 9. a) Schematic diagram of the SCMFC unit assembled with carbon cloth anode and catalyst loaded carbon cloth cathode; b) Polarization and power density plots of MFC using FeNC-D0.5 and Pt/C catalysts; c) The voltage output of MFC at external resistance of 1000 Ω; d) COD removal and CE of MFCs.

Besides the electricity generation from sewage, the substrate oxidation performance was also examined by the chemical oxygen demand (COD) removal efficiency. The substrate, containing sodium acetate media and domestic effluent (v/v = 3:1) collected from the sewage treatment plant, delivered an initial COD concentration of ≈3944 mg L^{-1}. During MFC operation for ≈140 h, approximately 91.6 ± 1.2% of the COD was removed using FeNC-D0.5-MFC (Figure 9d), which was obviously higher than that using the commercial Pt/C-MFC (89.9 ± 1.4%). In addition, the FeNC-D0.5-MFC exhibited a coulombic efficiency (CE) of 15.1 ± 0.4% at an external resistance of 1000 Ω, exceeding that of Pt/C-MFC (14.4 ± 0.7%). The high COD removal and CE were associated with the significant improvement of ORR activity and reaction kinetics of FeNC-D0.5, both of which were conductive to enhancing electron transport from microbe to electrode and the accumulation of anode biofilm.[71–73] The respectable catalytic properties of FeNC-D0.5 pose it as a promising cathode electrocatalyst in MFCs and ZABs. Its superiority in energy conversion devices originated from the compositional and structural merits, including the isolated Fe-N$_4$ moieties and high nitrogen content for promoting ORR, numerous mesopores for improving the exposure of catalytic active sites, well-balanced hydrophobic/hydrophilic surface, and petaloid porous nanosheet for facilitating the molecule/electrolyte diffusion.

3. Conclusion

In this study, a petal-like carbon nanosheet with well-dispersed atomic Fe sites was successfully constructed via a feasible silica-confined strategy. The desirable combination of silica protection and DTPA coordination offered a dual anchoring effect, mitigating Fe aggregation and achieving dense Fe-N$_4$ active sites. More importantly, the fluffy petaloid nanosheet coupled with an appropriate hydrophobicity and a large external surface area in FeNC-D0.5 achieved better O$_2$ diffusion and water management. These distinct characteristics ensured fast mass transfer and improved active site utilization. Owing to the maximized active site density, FeNC-D0.5 exhibited notable catalytic performance for ORR, prolonged durability, and stronger tolerance for methanol. Meanwhile, the high-activity of FeNC-D0.5 endowed the as-assembled ZAB and MFC with large power density (356 mW cm^{-2} and 1041.3 mW m^{-2}, respectively) and extended operational duration. Therefore, this work offers a viable route for maximizing the utilization of active sites towards high ORR kinetics and enabling the substitution of Pt-based catalysts.

Supporting Information

Supporting Information is available from the Wiley Online Library or from the author.

Acknowledgements

This research was supported by the National Natural Science Foundation of China (21673079, 21872056, and 21875070) and Guangzhou Municipal Science and Technology Project (20180410116).

Conflict of Interest

The authors declare no conflict of interest.

Keywords

air cathode, iron-nitrogen carbon, oxygen reduction reaction, single-atom catalysts

Received: October 4, 2020
Revised: November 24, 2020

---

[1] X. Tian, X. F. Lu, B. Y. Xia, X. W. Lou, *Joule* **2020**, *4*, 45.
[2] S. Ren, X. Duan, S. Liang, M. Zhang, H. Zheng, *J. Mater. Chem. A* **2020**, *8*, 6144.
[3] X. L. Tian, X. Zhao, Y. Q. Su, L. J. Wang, H. M. Wang, D. Dang, B. Chi, H. F. Liu, E. J. M. Hensen, X. W. Lou, B. Y. Xia, *Science* **2019**, *366*, 850.
[4] Y. Pan, C. Zhang, Z. Liu, C. Chen, Y. Li, *Matter* **2020**, *2*, 78.
[5] N. Ramaswamy, U. Tylus, Q. Jia, S. Mukerjee, *J. Am. Chem. Soc.* **2013**, *135*, 15443.
[6] A. Sarapuu, E. Kibena-Põldsepp, M. Borghei, K. Tammeveski, *J. Mater. Chem. A* **2018**, *6*, 776.
[7] A. Zitolo, V. Goellner, V. Armel, M. T. Sougrati, T. Mineva, L. Stievano, E. Fonda, F. Jaouen, *Nat. Mater.* **2015**, *14*, 937.
[8] X. Zhang, S. Zhang, Y. Yang, L. Wang, Z. Mu, H. Zhu, X. Zhu, H. Xing, H. Xia, B. Huang, J. Li, S. Guo, E. Wang, *Adv. Mater.* **2020**, *32*, 1906905.
[9] F. Li, G. F. Han, Y. Bu, H. J. Noh, J. P. Jeon, T. J. Shin, S. J. Kim, Y. Wu, H. Y. Jeong, Z. Fu, Y. Lu, J. B. Baek, *Angew. Chem., Int. Ed. Engl.* **2020**, *59*, 23678.
[10] J. Masa, A. Zhao, W. Xia, M. Muhler, W. Schuhmann, *Electrochim. Acta* **2014**, *128*, 271.
[11] S. Kattel, G. Wang, *J. Mater. Chem. A* **2013**, *1*, 10790.
[12] E. F. Holby, G. Wu, P. Zelenay, C. D. Taylor, *J. Phys. Chem. C* **2014**, *118*, 14388.
[13] R. Qin, K. Liu, Q. Wu, N. Zheng, *Chem. Rev.* **2020**, *120*, 11810.
[14] D. Zhao, Z. Zhuang, X. Cao, C. Zhang, Q. Peng, C. Chen, Y. Li, *Chem. Soc. Rev.* **2020**, *49*, 2215.
[15] T. Asset, P. Atanassov, *Joule* **2020**, *4*, 33.
[16] X. Wan, X. Liu, Y. Li, R. Yu, L. Zheng, W. Yan, H. Wang, M. Xu, J. Shui, *Nat. Catal.* **2019**, *2*, 259.
[17] W. Wei, X. Shi, P. Gao, S. Wang, W. Hu, X. Zhao, Y. Ni, X. Xu, Y. Xu, W. Yan, H. Ji, M. Cao, *Nano Energy* **2018**, *52*, 29.
[18] L. Jiao, R. Zhang, G. Wan, W. Yang, X. Wan, H. Zhou, J. Shui, S. H. Yu, H. L. Jiang, *Nat. Commun.* **2020**, *11*, 2831.
[19] G. Chen, P. Liu, Z. Liao, F. Sun, Y. He, H. Zhong, T. Zhang, E. Zschech, M. Chen, G. Wu, J. Zhang, X. Feng, *Adv. Mater.* **2020**, *32*, 1907399.
[20] L. Zhao, Y. Zhang, L. B. Huang, X. Z. Liu, Q. H. Zhang, C. He, Z. Y. Wu, L. J. Zhang, J. Wu, W. Yang, L. Gu, J. S. Hu, L. J. Wan, *Nat. Commun.* **2019**, *10*, 1278.
[21] M. X. Chen, M. Zhu, M. Zuo, S. Q. Chu, J. Zhang, Y. Wu, H. W. Liang, X. Feng, *Angew. Chem., Int. Ed. Engl.* **2020**, *59*, 1627.
[22] H. Zhang, H. T. Chung, D. A. Cullen, S. Wagner, U. I. Kramm, K. L. More, P. Zelenay, G. Wu, *Energy Environ. Sci.* **2019**, *12*, 2548.
[23] F. Jaouen, M. Lefevre, J. P. Dodelet, M. Cai, *J. Phys. Chem. B* **2006**, *110*, 5553.
[24] D. Malko, A. Kucernak, T. Lopes, *Nat. Commun.* **2016**, *7*, 13285.
[25] Y. Mun, S. Lee, K. Kim, S. Kim, S. Lee, J. W. Han, J. Lee, *J. Am. Chem. Soc.* **2019**, *141*, 6254.
[26] M. Qiao, Y. Wang, Q. Wang, G. Hu, X. Mamat, S. Zhang, S. Wang, *Angew. Chem., Int. Ed. Engl.* **2020**, *59*, 2688.
[27] L. Liu, G. Zeng, J. Chen, L. Bi, L. Dai, Z. Wen, *Nano Energy* **2018**, *49*, 393.
[28] Y. Chen, I. Kone, Y. Gong, A. Xie, H. J. Hu, D. D. Kong, J. Liu, Y. Tang, X. J. Yang, R. Pang, P. Y. Wan, *Carbon* **2019**, *152*, 325.
[29] Y. Wang, L. Tao, Z. Xiao, R. Chen, Z. Jiang, S. Wang, *Adv. Funct. Mater.* **2018**, *28*, 1705356.
[30] H. Shen, E. Gracia-Espino, J. Ma, H. Tang, X. Mamat, T. Wagberg, G. Hu, S. Guo, *Nano Energy* **2017**, *35*, 9.
[31] Y. J. Sa, D. J. Seo, J. Woo, J. T. Lim, J. Y. Cheon, S. Y. Yang, J. M. Lee, D. Kang, T. J. Shin, H. S. Shin, H. Y. Jeong, C. S. Kim, M. G. Kim, T. Y. Kim, S. H. Joo, *J. Am. Chem. Soc.* **2016**, *138*, 15046.
[32] D. Kim, N. P. Zussblatt, H. T. Chung, S. M. Becwar, P. Zelenay, B. F. Chmelka, *ACS Appl. Mater. Interfaces* **2018**, *10*, 25337.
[33] L. J. Yang, N. Larouche, R. Chenitz, G. X. Zhang, M. Lefevre, J. P. Dodelet, *Electrochim. Acta* **2015**, *159*, 184.
[34] Y. Wang, P. Zhu, H. Yang, L. Huang, Q. Wu, M. Rauf, J. Zhang, J. Dong, K. Wang, Z. Zhou, S. Sun, *ChemElectroChem* **2018**, *5*, 1914.
[35] Q. Zhao, J. An, S. Wang, Y. Qiao, C. Liao, C. Wang, X. Wang, N. Li, *ACS Appl. Mater. Interfaces* **2019**, *11*, 35410.
[36] H. Dong, H. Yu, X. Wang, Q. Zhou, J. Feng, *Water Res.* **2012**, *46*, 5777.
[37] H. Dong, H. Yu, X. Wang, *Environ. Sci. Technol.* **2012**, *46*, 13009.
[38] F. Zhang, G. Chen, M. A. Hickner, B. E. Logan, *J. Power Sources* **2012**, *218*, 100.
[39] W. Yang, X. Wang, M. Son, B. E. Logan, *J. Power Sources* **2020**, *465*, 228264.
[40] X. Yang, Y. Wang, G. Zhang, L. Du, L. Yang, M. Markiewicz, J.-y. Choi, R. Chenitz, S. Sun, *Appl. Catal., B* **2020**, *264*, 118523.
[41] G. Zhang, Y. Jia, C. Zhang, X. Xiong, K. Sun, R. Chen, W. Chen, Y. Kuang, L. Zheng, H. Tang, W. Liu, J. Liu, X. Sun, W.-F. Lin, H. Dai, *Energy Environ. Sci.* **2019**, *12*, 1317.
[42] X. Wang, C. Yuan, C. Shao, S. Zhuang, J. Ye, B. Li, *Environ. Res.* **2020**, *182*, 109011.
[43] K. Qu, Y. Zheng, S. Dai, S. Z. Qiao, *Nanoscale* **2015**, *7*, 12598.
[44] Y. Wang, S. Wang, R. Li, H. Li, Z. Guo, B. Chen, R. Li, Q. Yao, X. Zhang, H. Chen, Y. Li, K. Qu, Y. Zheng, *Carbon* **2020**, *162*, 586.
[45] D. Xia, X. Yang, L. Xie, Y. Wei, W. Jiang, M. Dou, X. Li, J. Li, L. Gan, F. Kang, *Adv. Funct. Mater.* **2019**, *29*, 1906174.
[46] W. Yang, X. Liu, X. Yue, J. Jia, S. Guo, *J. Am. Chem. Soc.* **2015**, *137*, 1436.
[47] H. Zhang, S. Hwang, M. Wang, Z. Feng, S. Karakalos, L. Luo, Z. Qiao, X. Xie, C. Wang, D. Su, Y. Shao, G. Wu, *J. Am. Chem. Soc.* **2017**, *139*, 14143.
[48] X. Zeng, J. Shui, X. Liu, Q. Liu, Y. Li, J. Shang, L. Zheng, R. Yu, *Adv. Energy Mater.* **2018**, *8*, 1701345.
[49] Y. Chen, S. Ji, S. Zhao, W. Chen, J. Dong, W. C. Cheong, R. Shen, X. Wen, L. Zheng, A. I. Rykov, S. Cai, H. Tang, Z. Zhuang, C. Chen, Q. Peng, D. Wang, Y. Li, *Nat. Commun.* **2018**, *9*, 5422.
[50] H. Chu, C. Shao, S. Qiu, Y. Zou, C. Xiang, F. Xu, L. Sun, *Inorg. Chem. Front.* **2018**, *5*, 225.
[51] C. Tang, H. F. Wang, X. Chen, B. Q. Li, T. Z. Hou, B. Zhang, Q. Zhang, M. M. Titirici, F. Wei, *Adv. Mater.* **2016**, *28*, 6845.
[52] K. Wu, X. Chen, S. Liu, Y. Pan, W. Cheong, W. Zhu, X. Cao, R. Shen, W. Chen, J. Luo, W. Yan, L. Zheng, Z. Chen, D. Wang, Q. Peng, C. Chen, Y. Li, *Nano Res.* **2018**, *11*, 6260.
[53] J. Wang, Y. Xu, B. Ding, Z. Chang, X. Zhang, Y. Yamauchi, K. C. W. Wu, *Angew. Chem., Int. Ed.* **2018**, *57*, 2894.
[54] J. Zhang, M. Zhang, Y. Zeng, J. Chen, L. Qiu, H. Zhou, C. Sun, Y. Yu, C. Zhu, Z. Zhu, *Small* **2019**, *15*, 1900307.
[55] C. Shao, S. Qiu, G. Wu, B. Cui, H. Chu, Y. Zou, C. Xiang, F. Xu, L. Sun, *Carbon Energy* **2020**, https://doi.org/10.1002/cey2.81.
[56] K. Yuan, D. Lutzenkirchen-Hecht, L. Li, L. Shuai, Y. Li, R. Cao, M. Qiu, X. Zhuang, M. K. H. Leung, Y. Chen, U. Scherf, *J. Am. Chem. Soc.* **2020**, *142*, 2404.
[57] S. Chen, N. Zhang, C. W. Narváez Villarrubia, X. Huang, L. Xie, X. Wang, X. Kong, H. Xu, G. Wu, J. Zeng, H. Wang, *Nano Energy* **2019**, *66*, 104164.

[58] Q. Wang, Y. Ji, Y. Lei, Y. Wang, Y. Wang, Y. Li, S. Wang, *ACS Energy Lett.* **2018**, *3*, 1183.
[59] D. Guo, R. Shibuya, C. Akiba, S. Saji, T. Kondo, J. Nakamura, *Science* **2016**, *351*, 361.
[60] Y. Chen, Z. Li, Y. Zhu, D. Sun, X. Liu, L. Xu, Y. Tang, *Adv. Mater.* **2019**, *31*, 1806312.
[61] F. Tang, H. T. Lei, S. J. Wang, H. X. Wang, Z. X. Jin, *Nanoscale* **2017**, *9*, 17364.
[62] L. Lin, Q. Zhu, A. Xu, *J. Am. Chem. Soc.* **2014**, *136*, 11027.
[63] D. Xia, F. Tang, X. Yao, Y. Wei, Y. Cui, M. Dou, L. Gan, F. Kang, *Carbon* **2020**, *162*, 300.
[64] K. H. Kangasniemi, D. A. Condit, T. D. Jarvi, *J. Electrochem. Soc.* **2004**, *151*, 125.
[65] M. Wu, Y. Liu, Y. Zhu, J. Lin, J. Liu, H. Hu, Y. Wang, Q. Zhao, R. Lv, J. Qiu, *J. Mater. Chem. A* **2017**, *5*, 11331.
[66] Y. Li, J. Huang, X. Hu, L. Bi, P. Cai, J. Jia, G. Chai, S. Wei, L. Dai, Z. Wen, *Adv. Funct. Mater.* **2018**, *28*, 1803330.
[67] G. Zhang, R. Chenitz, M. Lefevre, S. Sun, J.-P. Dodelet, *Nano Energy* **2016**, *29*, 111.
[68] L. Zou, Y. Qiao, C. M. Li, *Electrochem. Energy Rev.* **2018**, *1*, 567.
[69] Y. Du, F. Ma, C. Xu, J. Yu, D. Li, Y. Feng, L. Zhen, *Nano Energy* **2019**, *61*, 533.
[70] H. Yuan, Y. Hou, I. M. Abu-Reesh, J. Chen, Z. He, *Mater. Horiz.* **2016**, *3*, 382.
[71] K. Rabaey, G. Lissens, S. D. Siciliano, W. Verstraete, *Biotechnol. Lett.* **2003**, *25*, 1531.
[72] R. Wang, M. Yan, H. Li, L. Zhang, B. Peng, J. Sun, D. Liu, S. Liu, *Adv. Mater.* **2018**, *30*, 1800618.
[73] W. Xue, Q. Zhou, F. Li, B. S. Ondon, *J. Power Sources* **2019**, *423*, 9.